Flow structure and momentum transport for buoyancy driven mixing flows in long tubes at different tilt angles

J. Znaien,[a] F. Moisy, and J. P. Hulin
Université Pierre et Marie Curie-Paris 6 and Université Paris-Sud 11, CNRS, F-91405, Laboratoire FAST, Bât. 502, Campus Universitaire, Orsay F-91405, France

(Received 21 June 2010; accepted 8 February 2011; published online 16 March 2011)

Buoyancy driven mixing of fluids of different densities (ρ_1 and ρ_2) in a long circular tube is studied experimentally at the local scale as a function of the tilt angle from vertical ($15° \leq \theta \leq 60°$) and of the Atwood number $[10^{-3} \leq \mathrm{At} = (\rho_2 - \rho_1)/(\rho_2 + \rho_1) \leq 10^{-2}]$. Particle Image Velocimetry (PIV) and Laser Induced Fluorescence (LIF) measurements in a vertical diametral plane provide the velocity and the relative concentration (and, hence, density) fields. A map of the different flow regimes observed as a function of At and θ has been determined: as At increases and θ is reduced, the regime varies from laminar to intermittent destabilizations and, finally, to developed turbulence. In the laminar regime, three parallel stable layers of different densities are observed; the velocity profile is linear and well predicted from the density profile. The thickness of the intermediate layer can be estimated from the values of At and θ. In the turbulent regime, the density varies slowly with z in the core of the flow: there, transverse turbulent momentum transfer is dominant. As At decreases and θ increases, the density gradient β in the core (and, hence, the buoyancy forces) becomes larger, resulting in higher extremal velocities and indicating a less efficient mixing. While the mean concentration varies with time in the turbulent regime, the mean velocity remains constant. In the strong turbulent regime (highest At and lowest θ values), the transverse gradient of the mean concentration and the fluctuations of concentration and velocity remain stationary, whereas they gradually decay with time when turbulence is weaker. © *2011 American Institute of Physics*. [doi:10.1063/1.3560005]

I. INTRODUCTION

Buoyancy driven flows are widely encountered in meteorology, oceanography,[1] and volcanology[2] as well as in many practical applications in chemical,[3] petroleum, and environmental[4] engineering. Together with the density contrast characterized by the Atwood number (At), the angle θ of the mean flow with respect to vertical is a key parameter. Depending on this angle, a rich variety of flows may be observed, ranging from Rayleigh–Taylor instabilities[5] (vertical mean flow) to gravity currents (taking generally place on horizontal surfaces or weak slopes).[6–9] Many of these flows occur in confined geometries of tubes or open channels, particularly in industrial facilities; the confinement influences the development of unstable modes and, as a result, the properties of the flow.

The present work deals specifically with the buoyant flows of two fluids of different densities, ρ_1 and $\rho_2 (> \rho_1)$, in the strongly confined geometry of a long (3.6 m), narrow ($d = 20$ mm) tube. More precisely, we investigate by Particle Image Velocimetry (PIV) and Laser Induced Fluorescence (LIF) measurements the dependence of the local structure of these flows on the tilt angle θ from vertical and on the density contrast, characterized by the Atwood number $\mathrm{At} = (\rho_2 - \rho_1)/(\rho_2 + \rho_1)$. Practically, we use a symmetrical lock-exchange configuration,[10–12] in which the two fluids are initially separated by a removable wall, each of them occupying half of the length of the tube.

The flows investigated here involve a competition between different mechanisms. First, buoyancy forces due to the component of gravity parallel to the tube axis induce an interpenetration of the two fluids that flow in opposite directions. The resulting shear generates Kelvin–Helmholtz-like instabilities and, therefore, mixing across the tube section. This is opposed by the component of gravity transverse to the tube axis, which tends to keep the two fluids separated. The relative magnitude of these two effects depends both on θ and At.

Global measurements of the front velocity and of the variation of the mean concentration along the tube in such flows have been performed previously.[13,14] They show indeed that as θ decreases and At increases, there is a progressive transition from a separated laminar counterflow of the two fluids to weakly turbulent mixing. In another study,[15] local measurements were performed in the same geometry for one set of values of the angle ($\theta = 15°$) and the density contrast ($\mathrm{At} = 10^{-2}$) corresponding to well developed turbulent mixing. The experimental results were compared to direct three-dimensional (3D) numerical simulations: this work allowed us to validate the experimental measurements, to determine the main features of these flows, and to characterize (from the numerical simulations) the geometry of the 3D structures.

[a]Present address: Fluid Dynamics Laboratory, Department of Physics, Eindhoven University of Technology, P.O. Box 513, 5600 MB, Eindhoven, The Netherlands.

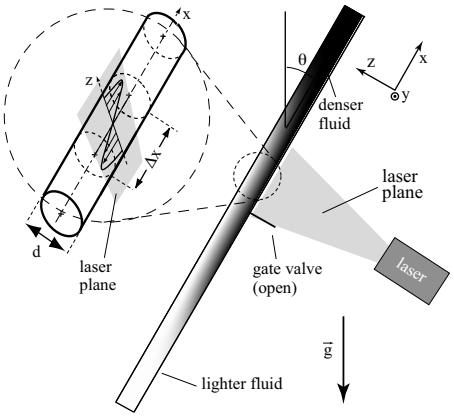

FIG. 1. Schematic front view of the experimental setup and of the lock-exchange flow. Inset: detailed oblique view of the region of the measurement window and of mean velocity field $\langle u \rangle(z)$.

Here, our objective is, instead, to focus on the influence of θ and At on the flow regimes and on the velocity and concentration fields. The experiments have been performed over a broad range of values of the control parameters, $15° \leq \theta \leq 60°$ and $10^{-3} \leq \mathrm{At} \leq 10^{-2}$. This allows us to observe very diverse flow regimes ranging from developed turbulence to intermittent and to laminar flows and to study their local spatial structure as well as their variation with time.

Practically, for each set of values of θ and At, the local concentration and velocity and their fluctuations are determined through different experiments as a function of the distance from the tube axis in the vertical measurement plane. These data give access to the dominant momentum transport terms and to the variation with θ and At of their relative magnitude in the different parts of the flow.

In the following, we identify first the different flow regimes in order to map their domains of existence in the (θ, At) plane: this is addressed through an analysis of the spatiotemporal characteristics of the local velocity and relative concentration. Then, the profiles of the mean concentration and of the longitudinal and transverse velocity components in both the laminar and the turbulent flow regimes are determined. Their variation with θ and At is analyzed together with the corresponding variations of the different measurable momentum transport terms. A particular attention is brought to the analysis of the stationarity of the mean velocities and of the fluctuations of the local velocity and concentration. Finally, we introduce models of the velocity field in the laminar regime and of the momentum balance in the turbulent one.

II. EXPERIMENTAL SETUP AND PROCEDURES

A. Setup

The experimental setup and procedure are described in Ref. 15. We use a long transparent polymethylmetacrylate tube (internal diameter: $d=20$ mm; length: $L=3.6$ m) with a tilt angle from vertical: $15° \leq \theta \leq 60°$ (see Fig. 1). The x axis coincides with that of the tube, the z and y axes are, respectively, located in the vertical diametral plane and perpendicular to it. Water and a denser $CaCl_2$-water solution fill the lower and upper halves of the tube length, respectively; they are initially separated by a gate valve that is opened at the origin time and located at $x=0$. Due to their low concentrations, the solutes induce only small variations of the viscosity ($\Delta\mu/\mu \simeq 0.06$); the viscosities of the two solutions will therefore be assumed to be equal to $\mu = 10^{-3}$ Pa s.

The local relative concentration $c(x,z,t)$ of the lighter fluid and the velocity components $u(x,z,t)$ and $w(x,z,t)$ are measured in the plane $y=0$, which is illuminated by a 2-mm-thick laser sheet ($\lambda = 532$ nm). Separate experiments using the LIF and PIV techniques are performed in order to obtain the concentration and velocity maps, respectively. For the LIF measurements, fluorescent rhodamin 6G dye, with concentration of 0.2 mg/l, is added to the lighter solution. For the PIV measurements, particles containing rhodamin B dye, with a maximum diameter of 50 μm and at a concentration of 0.3 mg/l, are added to both solutions. After the gate valve has been opened, LIF and PIV measurements are performed at constant time intervals equal to 0.5 and 0.25 s, respectively; the corresponding lengths Δx of the fields of view are 120 and 64 mm and their center is 300 mm above the gate valve.

The quantitative determination of the relative concentration of the fluids by the LIF technique is achieved by means of reference images obtained with the tube saturated by the pure fluids: the actual procedure is described in Ref. 16. The spatial resolution of the LIF images is 0.1 mm/pixel and that of the velocity maps is 0.4 mm. The relative uncertainty in the velocity is $\pm 2\%$ and the absolute one in the relative concentration is ± 0.03. The local density $\rho(x,z,t)$ of the mixture is estimated from the local relative concentration $c(x,z,t)$ by a linear interpolation between the respective densities ρ_1 and $\rho_2 = \rho + \Delta\rho$ of the lighter ($c=1$) and heavier ($c=0$) fluids.

B. Averaging procedure and notations

The flow is characterized quantitatively by the average values of the local concentration and velocity and by either the variance or the standard deviation of their fluctuations. In all cases, the averages are first performed over the length Δx of the measurement window; they are generally also performed over a time interval Δt and over an ensemble e of (typically 4) experiments corresponding to an identical set of control parameters. Averaging over a set of experiments reduces indeed the effect of the variability of the measurements from one experiment to another on the final results. The choice of Δt will be discussed separately for laminar and turbulent flows. The notation $\langle\ \rangle$ is used if the three types of averages mentioned above have been performed. Otherwise, the indices x, e, and/or t are mentioned explicitly. In some cases, an additional average is performed over the width Δz of the measurement window and referred to by the index z.

Note that the characteristic distances for the variation of the mean flow along x are on the order of the total length, $L \gg \Delta x$. Spatial variations of the velocity and of the concentration in the window Δx reflect therefore only local fluctuations. In the turbulent regime, these fluctuations have a key

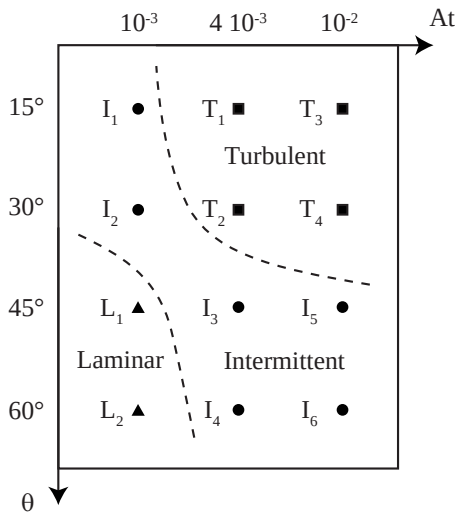

FIG. 2. Map of the flow regimes as a function of the tilt angle θ and of the Atwood number (At) for two fluids of same viscosity $\mu=10^{-3}$ Pa s in a 20 mm diameter tube. The symbols and labels mark pairs of values of At and θ corresponding to experiments performed in the different regimes during the present work: (■), T_i: turbulent; (●), I_i: intermittent; and (▲), L_i: laminar. The dotted lines are guides for the eye.

influence on mass and momentum transport. The fluctuations u' and w' of the components u and w of the velocity are defined as $u'=u-\langle u\rangle_{x,t}$ and $w'=w-\langle w\rangle_{x,t}$, respectively. Similarly, the fluctuations of the concentration are defined as $c'=c-\langle c\rangle_{x,t}$; in all cases, both the instantaneous local value and the average used to compute the fluctuations correspond to the same transverse distance z.

In the following, most plots and discussions use dimensionless variables, characterized with the symbol "~." Distances are normalized by the tube diameter d ($\tilde{z}=z/d$), whereas the velocity components u and w are normalized by the characteristic velocity $V_t=\sqrt{\mathrm{At}\ gd}$. This velocity scale reflects a balance between buoyancy and inertia and is thus relevant in the present flow regimes.[13] In the present work, V_t ranges from 15 to 47 mm/s, which corresponds to Reynolds numbers $300\leq \mathrm{Re}_t\leq 1000$ (with $\mathrm{Re}_t=V_t d/\nu$). Time is normalized by the ratio L/V_t so that $\tilde{t}=tV_t/L$ (the length L of the tube is used here because this normalization will mostly be used for characterizing transit times parallel to this length).

It is shown below that the flow is induced by the transverse variation of the density in the section of the tube, which is characterized by the difference $\delta\rho(x,z,t)=\rho(x,z,t)-\rho(x,0,t)$. The corresponding normalized variable is $\delta\tilde{\rho}=\delta\rho/(\langle\rho\rangle_{\Delta z}\mathrm{At})$. The factor $1/\mathrm{At}$ is included so that $\delta\tilde{\rho}$, like δc, is of the order of unity. Actually, for low density contrasts, one has $\delta\tilde{\rho}\simeq -2\delta c$.

III. MIXING FLOW REGIMES AND STATIONARITY OF THE FLOW

A. Flow regimes as a function of At and θ

The flow displays a variety of regimes, ranging from laminar to turbulent, depending on both control parameters θ and At: these regimes are mapped in Fig. 2 and are discussed in detail below. At the highest tilt angle ($\theta=60°$) and for a small At, there is a stable laminar flow. In contrast, for a tube close to vertical and a large density contrast, the flow is turbulent and strong transverse mixing occurs. Between these two extreme cases, one observes intermittent flows with both a few strongly turbulent bursts and time intervals during which the flow is laminar. Note that the boundaries between the different domains in Fig. 2 are just indications: no clear-cut transition between the different regimes is observed.

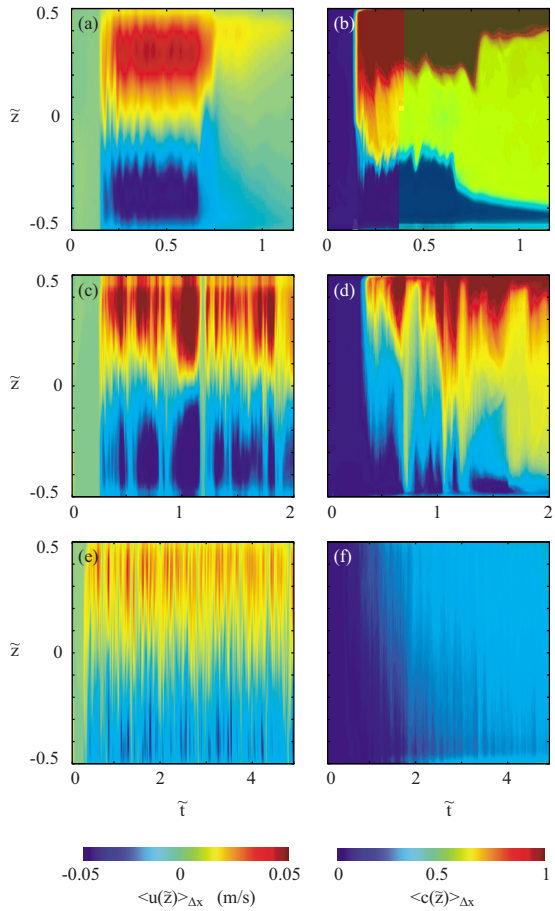

FIG. 3. (Color online) Spatiotemporal diagrams of the profiles of the velocity $\langle u\rangle_x(\tilde{z})$ (a), (c), and (e) and of the relative concentration $\langle c\rangle_x(\tilde{z})$ of the lighter fluid (b), (d), and (f) for three different pairs of values of θ and At. (a) and (b) $\theta=60°$, $\mathrm{At}=10^{-3}$ (case *L*2); (c) and (d) $\theta=45°$, $\mathrm{At}=4\times10^{-3}$ (case *I*3); and (e) and (f) $\theta=15°$, $\mathrm{At}=10^{-2}$ (case *T*3). Each vertical line corresponds to a time t and the color codes correspond to the respective values of $\langle u\rangle_x(\tilde{z})$ and $\langle c\rangle_x(\tilde{z})$ (see scales at the bottom of each column).

These flow regimes have been identified from the time sequences of both the velocity and the relative concentration fields. These sequences are summarized in Fig. 3 by the spatiotemporal diagrams of single experiments in the different regimes: the transverse profiles $\langle u\rangle_x(\tilde{z})$ of the velocity and $\langle c\rangle_x(\tilde{z})$ of the relative concentration of the lighter fluid at a time t are coded in false colors (or gray levels) on the corresponding lines of the diagram. As mentioned above, the velocity and concentration diagrams obtained for the same set of values of At and θ correspond to two different experiments. The overall characteristics of the variations of the velocity and concentration may therefore be compared but,

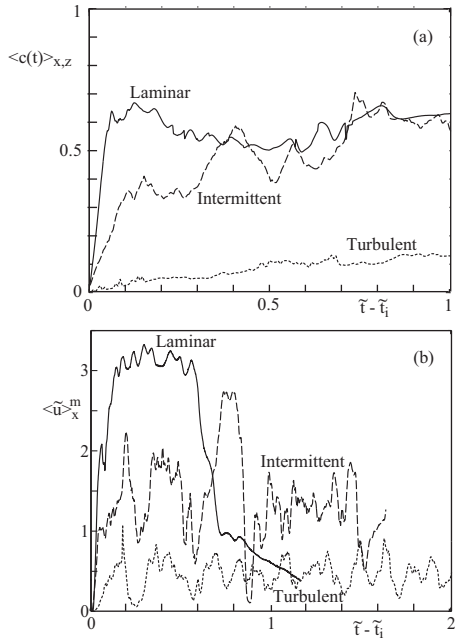

FIG. 4. Variation as a function of the dimensionless time $\tilde{t}-\tilde{t}_i$ of the averages over the measurement window of (a) the mean relative concentration $\langle c\rangle_{x,z}$ and (b) the half difference $\langle\tilde{u}\rangle_x^m$ between the positive and the negative velocity extrema. Solid line: case *L*2 (see Fig. 2); dashed line: *I*3; and dotted line: *T*3.

of course, not the individual events. From the diagrams of Fig. 3, the following features of the main types of flow regimes have been identified.

(a) Laminar regime—*L*2 [Figs. 3(a) and 3(b)]: the velocity profiles are almost stationary after the perturbation, due to the transit of the front, has died out ($\tilde{t}\geq 0.2$ s) and before the onset of the effect of the backfilling of the tube after the fronts reach the ends ($\tilde{t}\leq 0.7$). The concentration diagram displays three layers in the stationary regime. Some fluctuations of the boundaries are observed but they are too small to induce transverse mixing (except right behind the mixing front as mentioned above). Therefore, on the average, the concentration profiles remain stationary after an initial transient phase.

(b) Turbulent regime—*T*3 [Figs. 3(e) and 3(f)]: frequent fluctuations of short duration are visible in the velocity diagram. However, their distribution does not vary with time ($0.3\leq\tilde{t}\leq 5$), suggesting that the flow is statistically stationary. The concentration map displays similar fluctuations, but the mean value of the relative concentration varies with time.

(c) Intermittent regime—*I*3 [Figs. 3(c) and 3(d)]: the fluctuations of the velocity and of the concentration have a much larger amplitude and a longer duration than in the turbulent case. In several cases, an accelerating laminar counterflow is observed until a large turbulent burst is triggered. For instance, in Fig. 3(c), the increasingly dark blue and red shades for $0.9<\tilde{t}<1.15$ mark an acceleration of the counterflow of the two fluids until transverse mixing by turbulence (green shade for $\tilde{t}\simeq 1.15$) homogenizes the concentration. Similar bursts of turbulence have been reported in Refs. 17 and 18 in the case of turbidity currents.

B. Quantitative characterization of the flow regimes

As discussed above, the spatiotemporal diagrams of Figs. 3(a)–3(f) demonstrate qualitatively the features of the different flow regimes. A quantitative comparison is provided by the time variations of the average $\langle c\rangle_{x,z}$ of the concentration [Fig. 4(a)] and of the half difference $\langle\tilde{u}\rangle_x^m=(\langle\tilde{u}\rangle_x^{\max}-\langle\tilde{u}\rangle_x^{\min})/2$ between the positive and the negative extrema of the velocity [Fig. 4(b)]. Both figures correspond to the same set of experiments as in Fig. 3. They are plotted as a function of $\tilde{t}-\tilde{t}_i$, where $\tilde{t}_i$ is the normalized time at which the displacing fluid reaches the measurement window. Except in case *f*, $\tilde{t}_i$ is marked by a strong variation of the color shade in Fig. 3.

In the laminar regime (solid lines), the mean concentration $\langle c(t)\rangle_{x,z}$ rises rapidly to a value of the order of 0.5 after the arrival of the rising fluid in the measurement window for $\tilde{t}=\tilde{t}_i$, reflecting a symmetrical distribution of the two fluids. $\langle c(t)\rangle_{x,z}$ remains then almost constant with few fluctuations for $\tilde{t}-\tilde{t}_i>0.2$. The characteristic velocity $\langle\tilde{u}\rangle_x^m$ is also nearly constant until the onset of backfilling by the displacing fluid at both ends for $\tilde{t}-\tilde{t}_i\simeq 0.6$. These two variations suggest that an approximately stationary flow is reached for $\tilde{t}-\tilde{t}_i\in[0.2,0.6]$.

In the turbulent regime (dotted lines), the mean concentration increases slowly and continuously after the displacing fluid has reached the measurement window. This increase is consistent with the diffusive spreading of the profile of the mean concentration observed in previous experiments:[14] according to this latter work, the concentration $\langle c\rangle_{x,z}$ should increase here from 0 to 0.5, following an error function of $x/t^{1/2}$. The range of values of $\langle c\rangle_{x,z}$ is, however, too small here (typically 0–0.12) to identify precisely the law of variation. The characteristic velocity $\langle\tilde{u}\rangle_x^m$ displays large fluctuations but no drift of its mean value.

Finally, in the intermittent regime, the mean concentration increases faster toward 0.5 than in the turbulent one and displays a stepwise variation reflecting a few large mixing events [Fig. 4(a)]. In the variation of $\langle\tilde{u}\rangle_x^m$ [Fig. 4(b)], several fluctuations of much larger amplitude than in the turbulent case are observed.

The variations with time of the square of the concentration gradient along x, $\langle(\partial c/\partial\tilde{x})^2\rangle_{x,z}$, provide a very sensitive means of identifying the flow regimes from the concentration fields. In Fig. 5, the gradient is estimated from the finite difference of the local concentration over a distance of 2.5 mm along x. This choice represents a trade-off, allowing one to reduce the harmful effect of noise in the images at the cost of losing the influence of the smallest structures of the mixtures.

In the laminar regime, the initial transit of the front induces very large transient variations of the gradient, which becomes very low thereafter. In the turbulent regime, the

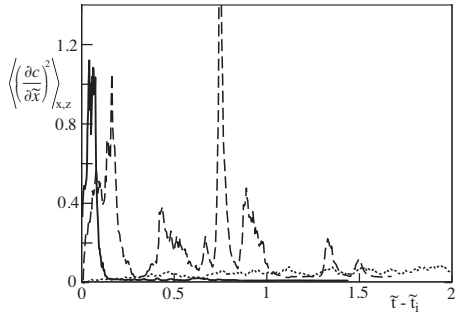

FIG. 5. Time dependence of the averages over the LIF measurement window of the squared longitudinal concentration gradient for three individual experiments in cases *L*2, *I*3, and *T*3. Time is counted after the displacement front has first reached the measurement window. The line styles have the same meaning as in Fig. 4.

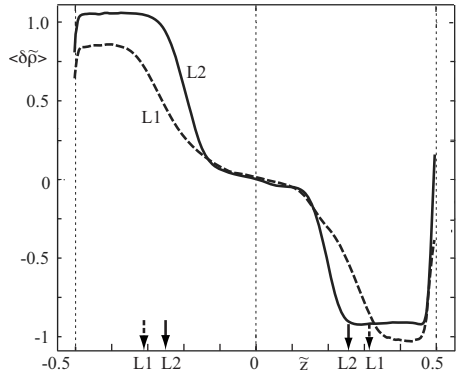

FIG. 6. Transverse profiles of the normalized local mean density contrast $\langle\delta\tilde{\rho}\rangle(\tilde{z})$ as a function of the transverse distance $\tilde{z}$ in the laminar flow regime in cases *L*1 (dashed line) and *L*2 (continuous line). Vertical arrows: locations of the boundaries of the intermediate mixed layer predicted from Eq. (9).

gradient increases slowly with time after the transit of the front and its value at long times is larger than in the laminar case.

In the intermittent regime, large mixing events are marked by large peaks of the gradient with amplitude close to that of the initial transient. These peaks are not symmetrical and display a steep rise as turbulence sets in the measurement window followed by a slow relaxation. Such peaks are not observed in the two other regimes and are a characteristic of the intermittent flows (Fig. 5). The minimum values are very low, confirming the occurrence of transient laminar flows.

In the following, we investigate the properties of the velocity and concentration fields and the characteristics of momentum transport in the mixing flows focusing on the laminar and the turbulent regimes only. The stationarity of these flows allows indeed for a joint analysis of the velocity and concentration fields obtained for same values of θ and At but from distinct experiments.

IV. LAMINAR FLOW REGIME

A. Experimental mean velocity and density profiles

In this section, we investigate first the mean transverse profiles of the density and of the velocity in the two laminar cases *L*1 and *L*2: more precisely, we plot averages taken over Δt, Δx and over the ensemble *e* of experiments corresponding to these two sets of control parameters. The interval $\Delta t=t_2-t_1$ used for the time average is determined in the following way: the lower boundary t_1 is chosen so that the perturbations due to the mixing zone right behind the front have died out. The upper boundary t_2 is such that the perturbations of the flow after the fronts have reached the end of the tube are not yet felt inside the measurement window.

Figure 6 displays the variation with the distance $\tilde{z}$ of the normalized density contrast $\langle\delta\tilde{\rho}\rangle(\tilde{z})=\langle\tilde{\rho}\rangle(\tilde{z})-\langle\tilde{\rho}\rangle(0)$. In both cases *L*1 and *L*2, these profiles have a three-layered structure. One observes a central layer of mixed fluid corresponding to a value of $\delta\tilde{\rho}$ decreasing slowly with $\tilde{z}$ from 0.1 to -0.1; it is surrounded by two layers of the nearly pure initial solutions with a density difference between them: $\langle\delta\tilde{\rho}\rangle(0.5)-\langle\delta\tilde{\rho}\rangle(-0.5)=-2[\langle\delta c\rangle(0.5)-\langle\delta c\rangle(-0.5)]\simeq-2$. These latter layers are broader at the largest tilt angle (case *L*2), and the transition from one layer to another is also much sharper. This suggests that mixing in the layered part (due to velocity and concentration fluctuations) and right behind the fronts is less efficient in case *L*2 than in case *L*1. One also notes an asymmetry between the parts of the curves corresponding to $\tilde{z}>0$ and $\tilde{z}<0$: a perfect symmetry is indeed only expected at the gate valve ($x=0$).

The differences between cases *L*1 and *L*2 are less pronounced for the velocity. Figure 7 shows that the profiles of the normalized longitudinal velocity $\tilde{u}$ in cases *L*1 and *L*2 coincide within less than 10%. The velocity $\tilde{u}$ varies linearly with $\tilde{z}$ at the center part of the pipe ($-0.3\lesssim\tilde{z}\lesssim0.3$) and displays a negative, steeper slope near the walls. This linear variation is coherent with the nearly constant density near the axis of the tube: in this region, one may expect indeed a pure shear flow driven by the two side layers. There is also a slight asymmetry between the parts of the curves corresponding to $\tilde{z}>0$ and $\tilde{z}<0$ but significantly weaker than for the density. The location $\tilde{z}_0$ of the extrema of the velocity from the axis is nearly the same for *L*1 and *L*2.

The transverse profiles of $\tilde{w}$ are also plotted with a vertical magnification of 10: in both cases *L*1 and *L*2, this transverse component is more than 100 times smaller than the

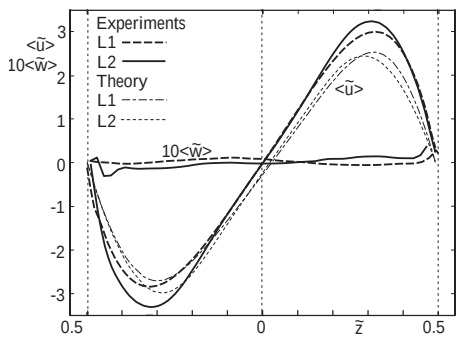

FIG. 7. Transverse profiles of the normalized mean velocity components $\langle\tilde{u}\rangle$ and $\langle\tilde{w}\rangle$ (magnified vertically by a factor 10) for cases *L*1 and *L*2. The symbols used for the experimental curves are the same as in Fig. 6. The dashed-dotted and dotted lines correspond to theoretical predictions from the density profiles of Fig. 6, respectively, in cases *L*1 and *L*2

longitudinal one. This is within the range of experimental errors, and $\tilde{w}$ may, therefore, be considered as negligible. Although the third velocity component v cannot be measured, this suggests that the flow is parallel to the x axis.

B. Relationship between velocity and density profiles

The above results demonstrate that in the laminar regime, the flow can be considered as parallel far enough from the front so that the perturbations it induces have relaxed. Since no external pressure gradient is applied, the longitudinal gradient is equal to the hydrostatic component corresponding to the average density. Also, convective momentum transport is negligible and viscous transport is the only relevant mechanism. If, in addition, the flow is stationary, the Navier–Stokes equation becomes

$$\langle \delta\rho \rangle(y,z) g \cos\theta = \mu(\partial_{y^2}\langle u\rangle + \partial_{z^2}\langle u\rangle) \tag{1}$$

or, using the dimensionless variables defined above,

$$\langle \delta\tilde{\rho} \rangle(\tilde{y},\tilde{z}) \cos\theta = \mathrm{Re}_t^{-1}(\partial_{\tilde{y}^2}\langle \tilde{u}\rangle + \partial_{\tilde{z}^2}\langle \tilde{u}\rangle). \tag{2}$$

For a parallel laminar flow, the transverse pressure gradient is only due to gravity and each flow section is in hydrostatic equilibrium: isodensity lines in a section are therefore horizontal, i.e., $\langle \delta\tilde{\rho} \rangle(\tilde{y},\tilde{z}) = \langle \delta\tilde{\rho} \rangle(0,\tilde{z})$. In this case, Eq. (2) can be rewritten as

$$\Delta_\perp \langle \tilde{u} \rangle = \mathrm{Re}_t \cos\theta \, \langle \delta\tilde{\rho} \rangle(\tilde{0},\tilde{z}), \tag{3}$$

in which $\Delta_\perp$ is the two-dimensional (2D) Laplacian operator in the (y,z) plane. Then, using the experimental profile $\langle \delta\tilde{\rho} \rangle(0,\tilde{z})$, a theoretical velocity field $\langle \tilde{u} \rangle(\tilde{y},\tilde{z})$ is computed by numerically integrating Eq. (3) using no-slip boundary conditions at the tube wall.

The velocity profiles $\langle \tilde{u} \rangle(0,\tilde{z})$ along the z axis obtained in this way are displayed in Fig. 7 for $\theta=45°$ and $\theta=60°$ (dotted and dashed-dotted lines). A good agreement with the experimental values (dashed and continuous lines) is obtained. This shows that in this regime, determining the density (or concentration) profile in the measurement plane provides a good prediction of the velocity profile at the center part of the flow section.

C. Relation between front velocity and velocity profiles

In this section, our objective is to relate the velocity V_f of the displacement fronts in the laminar regime to the profiles of the average velocity and density in the measurement window far from the fronts. For this purpose, we use a simplified model represented in Fig. 8 and reproducing approximately the concentration profiles of Fig. 6. The flow is divided longitudinally into three regions.

(1) Two regions of length Δx_f including the upper (lower) front and the mixing zone behind it. These regions propagate in opposite directions, reaching a constant velocity $\pm V_f$ after a short transient phase; they are assumed to be stationary in the moving reference frame of each front so that Δx_f is constant with time.

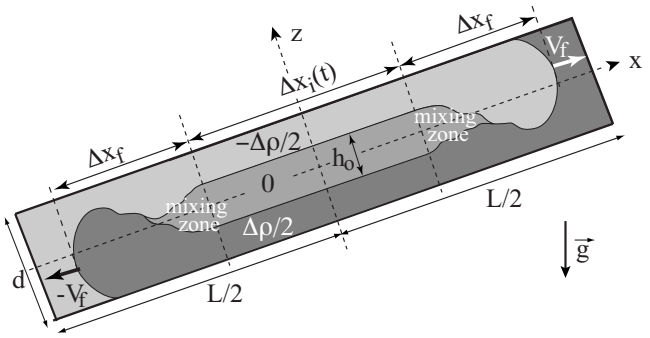

FIG. 8. Schematic view of the flow structure in the laminar layered regime. The scale in the z direction is expanded by a factor of 50 compared to the scale along x.

(2) A core region of length $\Delta x_i(t)$ where the flow is assumed to be laminar and parallel to x ($v=w=0$). There, no transverse mixing occurs and the transverse density profile is independent of x and t. In the model, the variation of the length Δx_i follows the motion of the fronts so that $d(\Delta x_i)/dt = 2V_f$ after the transient phase. In this latter region, one has pure light and heavy solutions, respectively, near the top and bottom of the section and mixed fluid near the center (as shown in Fig. 6, the density variations are generally not as sharp as in the schematic view of Fig. 8).

Figures 6 and 7 show that $\langle \delta\rho \rangle(y,z)$ and $\langle u \rangle(y,z)$ are odd functions of z; due to the lack of transverse mixing, they are assumed, in addition, to be independent of x. Then, one can write the equality between the mass flux through a section $x=cst$ (inside the interval Δx_i) and the variation per unit time of the total mass of fluid above this section as

$$\int\int_{\tilde{S}} \langle \delta\tilde{\rho} \rangle(\tilde{z}) \langle \tilde{u} \rangle(\tilde{z},\tilde{y}) d\tilde{z} d\tilde{y} = -\tilde{V}_f \tilde{S} \frac{\Delta\tilde{\rho}}{2} = -\frac{\pi \tilde{V}_f}{4}. \tag{4}$$

Here, the dimensionless density difference $\Delta\tilde{\rho}/2$ corresponds to the pure heavier fluid and is equal to 1 and $\tilde{S}=S/d^2 = \pi/4$ is the normalized section of the tube. Of course, the same relation might be obtained by computing the mass balance in the parts of the tube below the section $x=cst$.

We have used Eq. (4) to compute a theoretical front velocity in cases $L1$ and $L2$. The velocity field $\langle u \rangle(y,z)$ is computed like in Sec. IV B by numerically integrating Eq. (3). The resulting values of the front velocity V_f^{th} are listed in Table I. These theoretical predictions may be compared to the experimental values reported in Refs. 13 and 16 and also listed in Table I. Without using any adjustable parameter, the predicted values of V_f are lower than the experimental ones: this discrepancy has the same sign as in the simpler case of the counterflow of two fully separated fluids[13,19] but is larger (20%–30% instead of 16%). This difference likely reflects the crude description of the density profile used in the present section.

TABLE I. Characteristic parameters of the velocity and concentration fields for the two experiments corresponding to the laminar regime. $\langle\tilde{u}\rangle^m$: half difference between the positive and the negative extremal velocities in Fig. 7; $\tilde{z}_0$: mean absolute distance of the velocity extrema from the axis; $\tilde{V}_f^{\text{expt}}$: dimensionless front velocities from Ref. 13 for the same set of control parameters; $\tilde{V}_f^{\text{th}}$: dimensionless theoretical front velocities determined from Eq. (4); and $\tilde{h}_0$: dimensionless thickness of intermediate layer predicted from Eq. (9).

	*L*1	*L*2
θ	45°	60°
At	10^{-3}	10^{-3}
Re_t	300	300
$\langle\tilde{u}\rangle^m$	2.9	3.3
$\tilde{z}_0$	0.31	0.32
$\tilde{V}_f^{\text{expt}}$	0.72	0.74
$\tilde{V}_f^{\text{th}}$	0.57	0.55
$\tilde{h}_0^{\text{th}}$	0.62	0.53

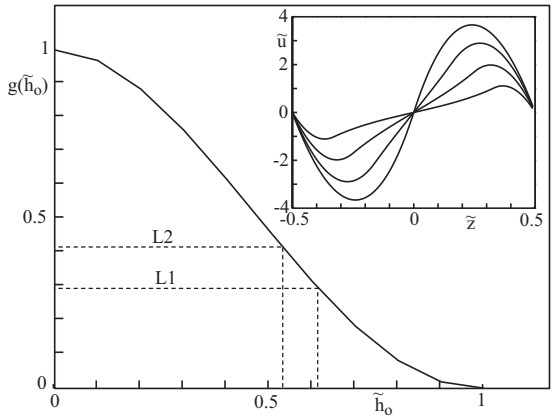

FIG. 9. Variation of the ratio $g(\tilde{h}_0)=\tilde{V}_f(\tilde{h}_0)/\tilde{V}_f(0)$ for a three-layered system as a function of the normalized thickness $\tilde{h}_0$ of the middle layer. Dotted lines: values of $\tilde{h}_0$ and $g(\tilde{h}_0)$ corresponding to cases *L*1 and *L*2. Inset: profiles of the normalized longitudinal velocity $\tilde{u}$ as a function of the transverse distance $\tilde{z}$. Values of $\tilde{h}_0$ corresponding to the different curves are, for decreasing amplitudes of the variations, 0, 1/3, 1/2, and 2/3.

D. Thickness of the mixing layer in the laminar regime

The objective of this section is now to predict theoretically the dependence of the density profile in the laminar regime on θ and Re_t. Practically, we model the actual profile by a central mixing layer of thickness $\tilde{h}_0$, where $\delta\tilde{\rho}=0$ between two layers of pure fluid with $\delta\tilde{\rho}=\pm 1$ (Fig. 8). In this simplified representation, the profile depends only on the parameter $\tilde{h}_0$. The corresponding variation of the dimensionless density $\delta\tilde{\rho}(x,z)$ is

$$\begin{cases} \delta\tilde{\rho}=1, & -1/2<\tilde{z}<-\tilde{h}_0/2 \\ \delta\tilde{\rho}=0, & -\tilde{h}_0/2\le\tilde{z}\le\tilde{h}_0/2 \\ \delta\tilde{\rho}=-1, & \tilde{h}_0/2<\tilde{z}<1/2. \end{cases} \tag{5}$$

This description represents well the overall variation of $\delta\tilde{\rho}(\tilde{z})$ but does not reproduce the smooth boundaries between the different layers (particularly at lower tilt angles such as $\theta=45°$ in Fig. 6). This variation also does not take into account the asymmetries between the parts of the profiles corresponding to $\tilde{z}<0$ and $\tilde{z}>0$: they should be in opposite directions for $x>0$ and $x<0$.

In the following, we develop first a procedure for computing theoretically the front velocity V_f^{th} as a function of $\tilde{h}_0$, Re_t, and θ when the variation of $\delta\tilde{\rho}(\tilde{z})$ corresponding to Eq. (5) is assumed. Then, for the given sets of values of Re_t and θ, we determine the thickness $\tilde{h}_0$ such that the predicted value of $\tilde{V}_f$ is equal to the experimental one.

In the first step, we compute V_f^{th} by applying the same procedures as in Secs. IV B and IV C to the density profile given by Eq. (5). This profile (and, therefore, the corresponding velocity field) is antisymmetrical with respect to $\tilde{z}$ and $\delta\tilde{\rho}=0$ at the center part of the tube. The left hand side of Eq. (4) may then be written as

$$\int\int_{\tilde{S}}\langle\delta\tilde{\rho}\rangle(\tilde{z})\ \langle\tilde{u}\rangle(\tilde{z},\tilde{y})\ d\tilde{z}d\tilde{y}=-2\int\int_{\tilde{S}_1}\langle\tilde{u}\rangle(\tilde{z},\tilde{y})\ d\tilde{z}d\tilde{y},$$

in which $\tilde{S}_1$ is the area of the region $(\tilde{h}_0/2<\tilde{z}<1/2)$ occupied by the pure light fluid, i.e., where $\delta\tilde{\rho}=-1$. Combining this relation with Eq. (4) leads to

$$\int\int_{\tilde{S}_1}\langle\tilde{u}\rangle(\tilde{z},\tilde{y})\ d\tilde{z}d\tilde{y}=\frac{\pi\tilde{V}_f}{8}. \tag{6}$$

The special case $\tilde{h}_0=0$ corresponds to a counterflow of the two pure fluids with no intermediate layer: this particular configuration is similar to the lock-exchange flow of immiscible fluids. In this case, $S_1=S/2$ and the mean velocity in S_1 is equal to the front velocity; its value $\tilde{V}_f^{\text{th}}(\tilde{h}_0=0)$ may be computed analytically[19] and is equal to $\text{Re}_t\ \cos\theta\ (1/16-1/2\pi^2)$.

In the more general case $\tilde{h}_0>0$, one has $\tilde{S}_1<\tilde{S}/2=\pi/8$ so that, from Eq. (6), the mean velocity in $\tilde{S}_1$ is larger than $\tilde{V}_f$. The velocity field $\tilde{u}(\tilde{z},\tilde{y})$ may be computed for any value of $\tilde{h}_0$ by numerically solving Eq. (3) like in Sec. IV B.

Velocity profiles $\tilde{u}(\tilde{z})$ in the plane $y=0$ obtained in this way are plotted in the inset of Fig. 9 for different values of $\tilde{h}_0$ in Eq. (5). When $\tilde{h}_0$ increases, the extrema of the velocities move toward the walls and their amplitude decreases, while a zone of low velocity gradient develops at the center: this reflects the stronger localization near the walls of the buoyancy forces and their smaller value.

The theoretical value $\tilde{V}_f^{\text{th}}(\tilde{h}_0)$ of the front velocity is then obtained by applying Eq. (6). Like $\tilde{V}_f^{\text{th}}(0)$, $\tilde{V}_f^{\text{th}}(\tilde{h}_0)$ is proportional to $\text{Re}_t\ \cos\theta$ for a constant $\tilde{h}_0$: the specific influence of $\tilde{h}_0$ may then be characterized by the ratio

TABLE II. Measured flow variables averaged over time (Δt), longitudinal distance (Δx), and experiments (e) for the sets T_i of control parameters corresponding to the turbulent regime. t_1: beginning; t_2: end of the averaging interval Δt (see Sec. II B). The characteristic velocity $\langle \tilde{u} \rangle^m$ and the distance $\tilde{z}_0$ are defined as in Table I.

	$T1$	$T2$	$T3$	$T4$
θ	15°	30°	15°	30°
At	4×10^{-3}	4×10^{-3}	10^{-2}	10^{-2}
Re_t	560 ± 10	560 ± 10	1000 ± 50	1000 ± 50
$\langle \tilde{u} \rangle^m$	0.56	0.90	0.37	0.60
$\tilde{z}_0$	0.36	0.37	0.38	0.39
$\tilde{V}_f$	0.24	0.33	0.16	0.24
$\langle \tilde{u} \rangle^m / \tilde{V}_f$	2.33	2.73	2.31	2.50
$\langle \tilde{u}'^2 \rangle_{\max}$	0.11	0.16	0.069	0.077
$\langle \tilde{w}'^2 \rangle_{\max}$	0.015	0.024	0.017	0.021
$\langle \tilde{u}'^2 \rangle_{\max} / \langle \tilde{w}'^2 \rangle_{\max}$	7.3	6.7	4.1	3.7
$\langle \tilde{w}'^2 \rangle_{\max}^{1/2} / \langle u \rangle_{\max}$	0.22	0.17	0.35	0.24
$\langle \tilde{\beta} \rangle_t$	0.39	0.66	0.22	0.38
$\langle c'^2 \rangle_{x,e}^{1/2}$	0.39	0.6	0.22	0.35
$\tilde{t}_1 - \tilde{t}_i$	0.6	0.7	1.2	0.7
$\tilde{t}_2 - \tilde{t}_i$	3.6	2.5	5.9	3.2

$$g(\tilde{h}_0) = \frac{\tilde{V}_f(\tilde{h}_0)}{\tilde{V}_f(0)}. \tag{7}$$

The value of $g(\tilde{h}_0)$ has been computed numerically for different thicknesses $\tilde{h}_0$ and the resulting variation is plotted in Fig. 9.

Combining the analytical value of $\tilde{V}_f^{\mathrm{th}}(0)$ with the definition of $g(\tilde{h}_0)$ leads to the following theoretical expression of the front velocity:

$$\tilde{V}_f^{\mathrm{th}}(\tilde{h}_0) = g(\tilde{h}_0)\ \mathrm{Re}_t\ \cos\theta \left(\frac{1}{16} - \frac{1}{2\pi^2}\right). \tag{8}$$

Since $g(\tilde{h}_0)$ is a monotonous function of $\tilde{h}_0$, this expression provides a theoretical value of $\tilde{h}_0$ when $\tilde{V}_f^{\mathrm{th}}$ is replaced by the experimental front velocity $\tilde{V}_f^{\mathrm{expt}}$ for the values of Re_t and θ of interest.

Such experimental values of $\tilde{V}_f^{\mathrm{expt}}$ for these laminar flows are reported in Table I and Ref. 13. For $\mathrm{Re}_t\ \cos\theta \lesssim 50$, $\tilde{V}_f$ varies linearly with $\mathrm{Re}_t\ \cos\theta$: this regime, in which V_f is determined by viscous dissipation along the full length of the flow, is observed for θ values larger than here and is therefore not considered.

For $\mathrm{Re}_t\ \cos\theta \gtrsim 50$, $\tilde{V}_f^{\mathrm{expt}}$ is nearly constant and will be taken equal to 0.73 (average of the values of Table I). Then, $g(\tilde{h}_0)$, Re_t, and $\cos\theta$ must satisfy

$$g(\tilde{h}_0)\mathrm{Re}_t\ \cos\theta = 0.73\left(\frac{16\pi^2}{\pi^2-8}\right) \simeq 61.5. \tag{9}$$

Since $g(\tilde{h}_0) \leq 1$, this equation may be solved for predicting $\tilde{h}_0$ from any set of values of Re_t and θ such that $\mathrm{Re}_t\ \cos\theta \geq 61.5$: this is similar to the range of values over which $\tilde{V}_f^{\mathrm{expt}}$ remains constant ($\mathrm{Re}_t\ \cos\theta \gtrsim 50$). Since $g(\tilde{h}_0)$ decreases monotonously with $\tilde{h}_0$, Eq. (9) implies that the thickness $\tilde{h}_0$ is larger at lower angles θ and higher Re_t.

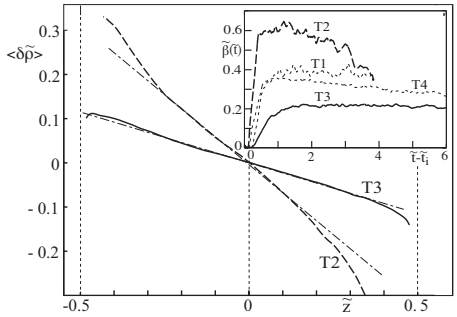

FIG. 10. Profiles of the normalized mean density contrast $\langle \delta\tilde{\rho} \rangle(\tilde{z}) = \langle \tilde{\rho} \rangle(\tilde{z}) - \langle \tilde{\rho} \rangle(0)$ as a function of the transverse distance $\tilde{z}$ in the turbulent flow regime. Continuous line: $T3$; dashed line: $T2$; and dashed-dotted lines: slopes of the profiles at $\tilde{z}=0$. Inset: variations of $\tilde{\beta}$ with $\tilde{t}$ for the different turbulent flows.

Applying Eq. (9) to cases $L1$ and $L2$ (see Table I) gives $g(\tilde{h}_0)=0.29$ and $g(\tilde{h}_0)=0.41$, respectively. From Fig. 9, the corresponding values of $\tilde{h}_0$ are $\tilde{h}_0^{L1}=0.62$ and $\tilde{h}_0^{L2}=0.53$. The predicted boundaries of the intermediate layer corresponding to these values of $\tilde{h}_0$ are indicated by the arrows in Fig. 6. The variation of $\tilde{h}_0$ with θ is correctly reproduced, but the predicted values are 20%–30% too high (taking the inflexion points of the profiles as the experimental boundaries); this is acceptable in view of the simple assumptions made here.

As the tilt angle θ decreases, the boundaries between the different layers become smoother, as can be seen in Fig. 6, and the width of the layers of each pure fluid at the top and bottom parts of the section becomes smaller. The validity of the three-layered model becomes then questionable.

V. TURBULENT FLOW REGIME

A. Average variables and stationarity of the flow

We shall now discuss the cases of large At and low θ values in which continuous turbulent mixing is observed. In this section, we characterize these flows by the average values of the local density and velocity components and by their fluctuations. The influence of the tilt angle θ and of the density contrast At is analyzed by comparing the results obtained in the four sets T_i of experiments corresponding to the turbulent regime (see Fig. 2). The results are listed in Table II and will be discussed below.

A major question is whether these flows can be considered as statistically stationary. The time dependence of the characteristic velocity $\tilde{u}_x^m$ and of the mean square concentration gradients displayed in Figs. 4(b) and 5 suggested qualitatively that the flow is statistically stationary. This key issue will be investigated quantitatively below for the different measured quantities.

1. Mean concentration profiles

Figure 10 displays the transverse profiles $\langle \delta\tilde{\rho} \rangle(\tilde{z})$ of the

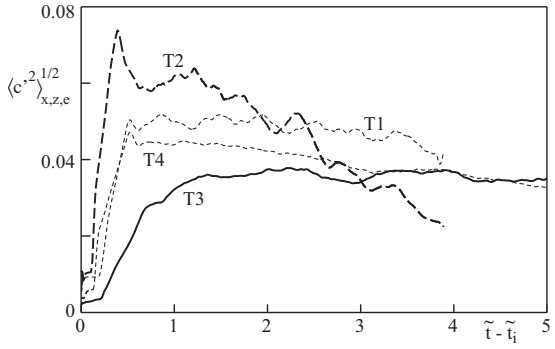

FIG. 11. Variation with the dimensionless time $\tilde{t}$ of the standard deviation $\langle c'^2\rangle^{1/2}$ of the local concentration (the same line patterns as in the inset of Fig. 10).

average local density contrast for cases $T2$ and $T3$ in the turbulent regime. As mentioned above, the average is taken over a set e of different experiments as well as over Δx and Δt. In this turbulent regime, the averaging interval $\Delta t = t_2 - t_1$ must be such that the flow can be considered as statistically stationary within it. Its boundaries t_1 and t_2 are determined from the variations with time of a parameter of the flow (averaged only over Δx and e): here, we selected the dimensionless absolute slope of the density profiles at $\tilde{z}=0$,

$$\tilde{\beta} = -\left[\frac{\partial\langle\delta\tilde{\rho}\rangle_{x,e}}{\partial\tilde{z}}\right]_{z=0}. \tag{10}$$

The product $\tilde{\beta}\cos\theta$ is indeed the normalized effective driving force of the flow and determines largely its properties [see Eq. (11) in Sec. V B]. The global density difference plays a significant role only in the initial phase of the interpenetration flow, while the influence of the local variations across the tube section becomes dominant as soon as mixing takes place.

For a stationary flow, $\tilde{\beta}$ should therefore remain constant with time even though the mean concentration (and density) varies: its variations are plotted in the inset of Fig. 10. For experiments $T1$ and $T3$ at $\theta=15°$, $\tilde{\beta}$ varies by less than 10%: the flow can therefore be considered as statistically quasistationary after the initial phase. For $\theta=30°$, in the less turbulent case $T2$, $\tilde{\beta}$ decreases by 40% in the later stages of the flow ($\tilde{t}\geq 2$) and also slightly in case $T4$: the flow is then only quasistationary at earlier times. Practically, we select as the lower boundary of the averaging interval Δt the time t_1 at which the curve reaches its maximum which marks the end of the initial phase. The upper boundary t_2 is chosen as the time corresponding to either 90% of this maximum or to the end of the recording; this also ensures that the measurements are not influenced by the backfilling front. The corresponding normalized values $\tilde{t}_1 - \tilde{t}_i$ and $\tilde{t}_2 - \tilde{t}_i$ are listed in Table II; they have been used to compute the averages in the main graph of Fig. 10. For consistency, the same values of $\tilde{t}_1 - \tilde{t}_i$ and $\tilde{t}_2 - \tilde{t}_i$ are then retained for computing the time averages of other variables.

The slope of this average density profile at $\tilde{z}=0$ (dashed-dotted lines in the main graph Fig. 10) is larger by a factor of 3 for $T2$ than for $T3$, while the domain of linear variation with $\tilde{z}$ is narrower ($d/3$ instead of $d/2$). This indicates that turbulent mixing has a reduced efficiency for $T2$ and is more localized at the center of the tube. Moreover (still for $T2$), the slope increases more strongly near the walls and $\langle\delta\tilde{\rho}\rangle(\tilde{z})$ reaches higher absolute values. In cases $T1$ and $T4$, the average slopes $\langle\tilde{\beta}\rangle_t$ are intermediate between those for $T2$ and $T3$ (see Fig. 10 and Table II). This shows that in the present work, the variations of At and θ have a similar influence on the concentration field.

This variation of $\langle\tilde{\beta}\rangle_t$ with θ has an important consequence: increasing θ reduces the gravity component $g\cos\theta$ along the tube at the origin of the flow. However, the effective driving force is not determined solely by $\cos\theta$ but by the product $\langle\tilde{\beta}\rangle\cos\theta$ (using normalized variables). Here, the increase of $\tilde{\beta}$ with θ due to less effective mixing is observed to dominate the variation of $g\cos\theta$, which leads to an increase of the effective local driving force.

2. Concentration fluctuations

The stationarity of the concentration fluctuations is analyzed from Fig. 11, displaying the variation of the standard deviation $\langle c'^2\rangle^{1/2}_{x,e}$ as a function of the normalized time $\tilde{t}$ for the different experiments (the standard deviation provides here a correct characterization of these fluctuations because they are found to be normally distributed). All four curves are strikingly similar to those corresponding to the same case in the inset of Fig. 10: this suggests that the fluctuations are slaved to the effective force term $\tilde{\beta}$. In cases $T1$ and $T3$ ($\theta=15°$), the value of $\langle c'^2\rangle^{1/2}_{x,e}(\tilde{t})$ is nearly constant, which confirms that stationarity is indeed satisfied in this case. This contrasts with the strong decay observed for $T2$ and the weaker one for $T4$.

The stationarity in cases $T1$ and $T3$ implies that the concentration gradients are continuously enhanced by the arrival of fluids of different concentrations from both sides of the tube section: this compensates for their attenuation by the mixing effect of turbulence. The maximum value of $\langle c'^2\rangle^{1/2}_{x,e}$ is three times lower for $T3$ than for $T2$ (see Table II), which confirms that the mixing efficiency is higher for $T3$.

3. Mean velocity profiles

In contrast to β and $\langle c'^2\rangle^{1/2}$, the mean velocity profiles can be considered as independent of time in all cases. This is shown in the inset of Fig. 12 in which the characteristic velocity $\langle u\rangle^m_{x,e}$, defined as in Sec. III A, is plotted as a function of the dimensionless time $\tilde{t}$. In all four cases T_i, $\langle u\rangle^m_{x,e}$ can be considered as constant within experimental error after a transient initial variation. This difference may reflect a different nature of these quantities: β and $\langle c'^2\rangle^{1/2}$ are defined purely locally, while the mean velocity is determined by the distribution of the two fluids all along the mixing zone.

Another difference with the density profiles of Fig. 10 is that, although the extremal values are different, the profiles $\tilde{u}(\tilde{z})$ displayed in the main graph of Fig. 12 for $T2$ and $T3$ are very similar. In both cases, the variation of $\tilde{u}$ with $\tilde{z}$ is linear

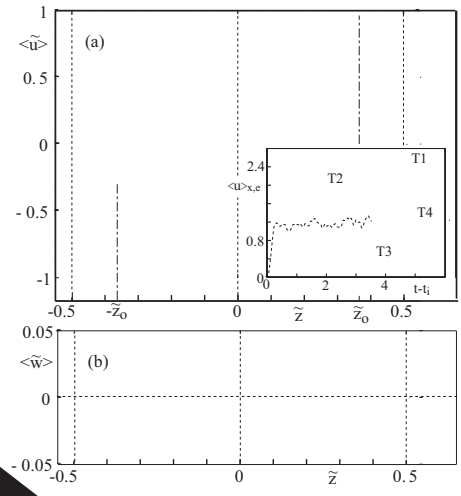

e velocity are at
and $\tilde{u}$ de-

n for

window, their velocity V_f is, like in the laminar regime, closely related to the longitudinal velocities near the gate valve. In order to achieve mass conservation, the large value of the ratio $\langle\tilde{u}\rangle_{\max}/V_f$ requires that recirculation flows be present in the vicinity of the front, as discussed by other authors.[7,21,22]

bulent velocity fluctuations

l important characteristics are the intensity and
he turbulence: they are characterized by the
uare components $\langle\tilde{w}'^2\rangle(\tilde{z})$ and $\langle\tilde{u}'^2\rangle(\tilde{z})$ of
w' defined in Sec. II B. These are
function of the distance $\tilde{z}$ for the
the values and transverse pro-
agnitude of $\langle\tilde{u}'^2\rangle(\tilde{z})$ and,
t fluctuations are sig-
may be related to
the mean flow
ponent u'
ported
for

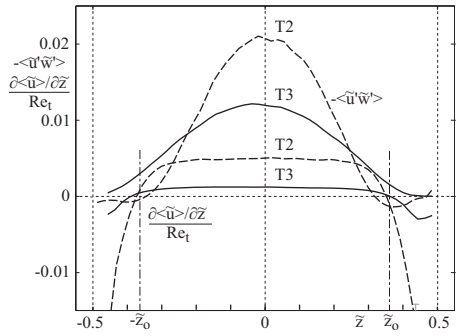

FIG. 14. Turbulent (top curves) and viscous (bottom curves) in-plane normalized stress components for the cases $T2$ and $T3$. The line patterns are the same as in Fig. 10. The vertical dashed-dotted lines mark the location of the extrema of the mean velocity.

The variations with time of the squared magnitude $\langle \tilde{w}'^2 \rangle_{x,e}(\tilde{z}=0)$ of the transverse velocity fluctuations are displayed in Fig. 13(b): these variations are much more similar to those of β and of the standard deviation of the concentration fluctuations $\langle c'^2 \rangle^{1/2}$ than to those of the maximum velocity. The squared magnitude remains approximately constant for $T1$ and $T3$, while it decreases significantly for $T2$ for $\tilde{t} \geq 1.5$ and slower for $T4$. The reduced value of the parameter β characterizing the effective driving force of the flow seems to lead therefore to weaker velocity and concentration fluctuations.

B. Momentum transport in the turbulent regime

1. Viscous and turbulent transport

A key information on the mixing flow is the relative magnitude of the laminar and turbulent momentum transport terms. The global momentum balance of the flow is expressed by the x component of the normalized Reynolds equation,[26]

$$\delta\tilde{\rho}(\tilde{z})\cos\theta = -\langle \tilde{w} \rangle \partial_{\tilde{z}} \langle \tilde{u} \rangle - \partial_{\tilde{y}} \langle \tilde{u}' \tilde{v}' \rangle - \partial_{\tilde{z}} \langle \tilde{u}' \tilde{w}' \rangle + \mathrm{Re}_t^{-1} \partial_{\tilde{z}^2} \langle \tilde{u} \rangle. \quad (11)$$

This expression contains only terms shown to be large enough to be relevant in case $T3$ by the numerical simulations and experiments reported in Ref. 15. It is assumed that these same terms are the meaningful ones in the other cases: $T1$, $T2$, and $T4$.

The only viscous and turbulent terms of Eq. (11) measurable experimentally are $\mathrm{Re}_t^{-1} \partial_{\tilde{z}^2} \langle \tilde{u} \rangle$ and $-\partial_{\tilde{z}} \langle \tilde{u}' \tilde{w}' \rangle$, respectively. They represent the derivatives with respect to z (actually a divergence) of the viscous and turbulent stress components: $\mathrm{Re}_t^{-1} \partial_{\tilde{z}} \langle \tilde{u} \rangle$and $-\langle \tilde{u}' \tilde{w}' \rangle$.

The term $-\partial_{\tilde{y}} \langle \tilde{u}' \tilde{v}' \rangle$ corresponds to the out-of-plane turbulent transport: in case $T3$, it was found numerically to vary with $\tilde{z}$ like the in-plane one while being about 40% lower. Finally, $-\langle \tilde{w} \rangle \partial_{\tilde{z}} \langle \tilde{u} \rangle$ corresponds to transport by the mean transverse velocity $\langle w \rangle$; it also had a dependence on $\tilde{z}$ similar to the in-plane turbulent term.

The variation of the turbulent stress $-\langle \tilde{u}' \tilde{w}' \rangle$ with $\tilde{z}$ will therefore be considered as representative of that of the other nonmeasurable convective terms. It is compared in Fig. 14 to the variation of the viscous stress: $\mathrm{Re}_t^{-1} \partial_{\tilde{z}} \langle \tilde{u} \rangle$ in cases $T2$ and $T3$. Also, the values of these two terms at $\tilde{z}=0$ are compared in Table III for all turbulent cases T_i.

TABLE III. Flow and momentum transport parameters in the wall and core regions for the four turbulent flow cases.

	$T1$	$T2$	$T3$	$T4$
θ	15°	30°	15°	30°
At	4×10^{-3}	4×10^{-3}	10^{-2}	10^{-2}
Re_t	560 ± 10	560 ± 10	1000 ± 50	1000 ± 50
Boundary between wall and core regions				
$\langle \delta\tilde{\rho} \rangle(\tilde{z}_0)$	0.16	0.27	0.11	0.14
$\tilde{u}^m_{\mathrm{expt}}$	0.56	0.90	0.37	0.60
$\tilde{u}^m_{\mathrm{est}}$	1.0	1.5	0.85	0.8
Core region				
$-\langle \overline{\tilde{u}'\tilde{w}'} \rangle(0)$	0.014	0.021	0.012	0.016
$1/\mathrm{Re}_t \ \partial_{\tilde{z}} \langle \tilde{u} \rangle(0)$	3.3×10^{-3}	5.0×10^{-3}	1.3×10^{-3}	1.6×10^{-3}
$\tilde{l}_m(0)$	0.062	0.051	0.094	0.071
$\beta\cos\theta\ \tilde{z}_0^2/2$	0.0245	0.039	0.015	0.025
Buoyancy term / Transport terms	1.41	1.50	1.15	1.42

In the core of the flow, the turbulent stress is always larger than the viscous one: however, their ratio (turbulent/viscous) is larger for $T3(\simeq 12)$ than for $T2(\simeq 4)$. This stronger influence of the viscosity for $T2$ is confirmed by the narrower domain over which the turbulent term is dominant ($-0.3 \leq \tilde{z} \leq 0.3$ for $T2$ against $-0.4 \leq \tilde{z} \leq 0.4$ for $T3$).

In both cases, the turbulent term reaches its maximum on the tube axis but its variations near the walls differ. For $T3$, it decreases monotonously with $|\tilde{z}|$ and is nearly zero for $|\tilde{z}| \geq 0.45$. For $T2$, it displays a negative overshoot beyond $|\tilde{z}| \simeq 0.32$: this corresponds to a local turbulent momentum transfer component oriented toward the walls in addition to the viscous one. Also, the turbulent term is of the same order as the mean square $\langle \tilde{w}'^2 \rangle_t$ of the transverse fluctuations but significantly smaller than $\langle \tilde{u}'^2 \rangle_t$.

2. Turbulent transport characterization by the mixing length model

In an attempt to quantitatively characterize the relation between the momentum flux $-\langle \tilde{u}' \tilde{w}' \rangle$ and the streamwise velocity field $\langle u \rangle$, we computed a dimensionless mixing length $\tilde{l}_m$ by

$$-\langle \tilde{u}' \tilde{w}' \rangle = \tilde{l}_m^2(\tilde{z}) \partial_{\tilde{z}} \langle \tilde{u} \rangle |\partial_{\tilde{z}} \langle \tilde{u} \rangle|. \quad (12)$$

This approach was selected because l_m was found to be constant in several types of free shear flows[26] including stratified flows similar in several respects to ours.[1] This definition of $\tilde{l}_m$ is only meaningful if $-\langle \tilde{u}' \tilde{w}' \rangle$ and $\partial_{\tilde{z}} \langle \tilde{u} \rangle$ have the same sign, which is satisfied in the turbulent core.

The experimental variations of the normalized mixing length $\tilde{l}_m$ as a function of $\tilde{z}$ for the sets of experiments T_i are plotted in Fig. 15; all data correspond to the core of the flow

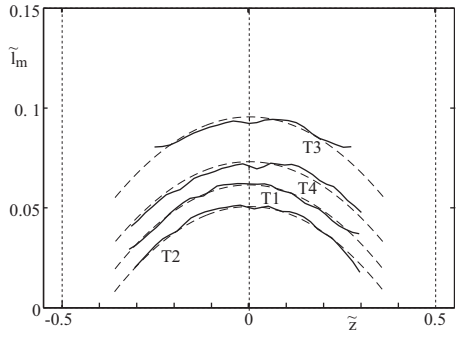

FIG. 15. Variation of the dimensionless mixing length $\tilde{l}_m$ from Eq. (12) as a function of $\tilde{z}$ for four different turbulent cases (see labels). Continuous lines: experimental data; dashed lines: fit by a quadratic variation (shown as a guide to the eye). The values of $\tilde{l}_m$ for $\tilde{z}=0$ are listed in Table III.

where turbulent transport is dominant. The length $\tilde{l}_m$ is of the order of 1/10 of the width of the shear layer, which is the same order of magnitude as for free shear flows. However, in contrast to Ref. 1, $\tilde{l}_m$ may only be considered as approximately constant with $\tilde{z}$ in the strong mixing case $T3$. In all other cases, the variations of $\tilde{l}_m$ with $\tilde{z}$ are better fitted by a quadratic dependence and the value of $\tilde{l}_m$ at a given point depends both on At and θ. In contrast to the conclusions of Ref. 1, the mixing length description does not approach well most of the turbulent mixing flows investigated here, perhaps due to the larger influence of the channel walls.

C. Momentum balance in the different regions of the turbulent flow

1. Characteristics of the different regions of the flow

As shown in the previous parts, flow in the turbulent regime can be modeled approximately as a turbulent mixing zone at the center surrounded by two channels with more concentrated solutions near each wall. The size of the channels and the absolute values of $\langle \delta\rho \rangle$ are larger at lower At and higher angles θ. In these three regions, the flux of momentum (equal and opposite to the stress) reflects different dominant mechanisms and is oriented differently.

(a) At the center part, turbulent momentum transport is dominant and takes place internally between the upper and the lower halves of the core region. Positive momentum produced by buoyancy forces in the upper half of the section and negative momentum produced in the lower one are transported in opposite directions through the plane $z=0$.

(b) In the near-wall regions, the global flux is oriented toward the walls and is dominantly viscous; in case $T2$, the negative overshoot of the turbulent stress tensor in the regions of the walls represents an additional turbulent momentum flux component adding up to the viscous one.

The boundaries between these two types of regions should correspond to the point at which the sum of the turbulent and viscous momentum flux goes to zero. The corresponding distances to the axis in cases $T2$ and $T3$ are $|\tilde{z}| \simeq 0.35$ ($T2$) and $|\tilde{z}| \simeq 0.4$ ($T3$): they turn out to be close to the location z_0 of the velocity extrema. A more precise evaluation would require a determination of the other momentum transport terms.

2. Momentum balance and velocity profiles in the wall regions

In these wall regions that, as discussed above, correspond to $\tilde{z}_0 < |\tilde{z}| \leq 1/2$, momentum transport may be assumed to be purely viscous. In order to check whether this assumption is compatible with the measured values of $\delta\tilde{\rho}(\tilde{z}_0)$ and $\tilde{u}(\tilde{z}_0)$, it is assumed, for simplicity, that the flow is locally two dimensional without momentum transfer along y. One also assumes that the density contrast $\delta\tilde{\rho}$ retains the same value as for $\tilde{z}=\tilde{z}_0$. The equation of motion reduces then to

$$\langle \delta\tilde{\rho} \rangle(\tilde{z}_0) \cos\theta = \mathrm{Re}_t^{-1} \ \partial_{\tilde{z}^2} \langle \tilde{u} \rangle. \tag{13}$$

Since the velocity gradient $\partial\tilde{u}/\partial z$ is zero for $\tilde{z}=\pm\tilde{z}_0$ and the velocity is zero at the wall ($\tilde{z}=\pm 1/2$), the resulting parabolic profile $\tilde{u}(\tilde{z})$ is the same as for the gravity driven flow of a viscous liquid film of density $\langle \delta\tilde{\rho} \rangle(\tilde{z})$ and thickness $(1/2-\tilde{z}_0)$ on a tilted wall. Integrating Eq. (13) with these boundary conditions leads to an estimate of the maximum velocity equal in this case to the characteristic velocity $\langle \tilde{u} \rangle^m$ defined in Sec. III A,

$$\langle \tilde{u} \rangle^m_{\mathrm{est}} = -\langle \delta\tilde{\rho} \rangle(\tilde{z}_0) \frac{\mathrm{Re}_t \cos\theta}{2} \left(\tilde{z}_0 - \frac{1}{2} \right)^2. \tag{14}$$

The corresponding values are listed in Table III and are, on the average, 70% higher than the experimental ones: this may reflect the influence of the remaining turbulent fluctuations in this zone and of velocity gradients along y due to the curvature of the wall.

3. Turbulent core region

Like in the wall region, we use a simplified version of Eq. (11),

$$\delta\tilde{\rho}(\tilde{z}) \cos\theta = -\partial_{\tilde{z}} \langle \tilde{u}' \tilde{w}' \rangle + \mathrm{Re}_t^{-1} \ \partial_{\tilde{z}^2} \langle \tilde{u} \rangle. \tag{15}$$

Both terms $-\langle \tilde{w} \rangle \partial_{\tilde{z}} \langle \tilde{u} \rangle$ and $-\partial_{\tilde{y}} \langle \tilde{u}' \tilde{v}' \rangle$ representing, respectively, momentum transport by the mean transverse velocity $\langle w \rangle$ and by the out-of plane velocity fluctuations v' have been neglected.

Unlike in the viscous case, however, the relation between the turbulent stress and the velocity gradients is not straightforward: the discussion of Sec. V B 2 has shown indeed that the mixing length l_m depends not only on the set of parameters T_i investigated but also on the transverse distance $\tilde{z}$. Therefore, rather than attempting to predict the local velocity profile, we shall investigate the global momentum balance of the flow: this allows one both to check the consistency of the density and velocity measurements and also to estimate the relative influence of the 3D transport terms. Integrating Eq. (15) between 0 and $\tilde{z}_0$ (i.e., over the turbulent core), after approximating $\delta\tilde{\rho}(\tilde{z})$ by $-\beta\tilde{z}$ leads to

$$\beta \cos\theta \frac{\tilde{z}_0^2}{2} = -\langle \tilde{u}'\tilde{w}' \rangle(0) + \mathrm{Re}_t^{-1} \partial_{\tilde{z}} \langle \tilde{u} \rangle(0) \tag{16}$$

since the sum of the momentum fluxes cancels out at $\tilde{z}=\tilde{z}_0$. This represents, under the above assumptions, the global momentum balance in a thin slice of fluid centered on the plane $y=0$ and extending from $z=0$ to $z=z_0$.

The ratio of the buoyancy term at the left and of the sum of the transport terms at the right is given in Table III. This ratio varies from 1.15 in case $T3$ to 1.5 in case $T2$. This confirms that the description of the flow in the core as a 2D turbulent shear flow is more valid in the more strongly turbulent case $T3$; in the others, the additional terms representing transport by the transverse mean velocity and by the out-of-plane fluctuations play a significant part in the global momentum balance.

VI. DISCUSSION AND CONCLUSION

It is apparent from the present work that the characteristics of viscous/turbulent momentum and mass transport in these mixing flows differ strongly from those of pressure driven flows[27] in similar channels. Here, the streamwise pressure gradient is purely hydrostatic and flow is driven by buoyancy forces due to the transverse gradients of the fluid density. The observed flow regimes depend on the relative influence of mixing by shear driven instabilities and of segregation by the transverse gravity. More precisely, as the Atwood number (At) increases and the tilt angle θ is reduced, a transition from laminar quasibidimensional flow to intermittent destabilizations and, finally, to developed turbulence is observed.

While these flow regimes are easily identified qualitatively, their influence on the different parameters and statistical moments characterizing the velocity and concentration fields may be variable. For instance, the shape of the mean velocity profile remains qualitatively the same in the laminar and turbulent regimes (linear variation at the center with two off-axis extrema), while the normalized maximum velocity varies. The variation of the transverse flux of momentum with $\tilde{z}$ is also qualitatively similar in the laminar and turbulent regimes: it is highest on the tube axis and becomes zero near the extrema of the velocity. Also, in both regimes, in the core region between the two extrema ($|\tilde{z}|<\tilde{z}_0$), momentum is exchanged internally between the two halves of the flow section (either by viscous diffusion or by turbulent fluctuations when present). In the wall region ($\tilde{z}_0<|\tilde{z}|<d/2$), viscous momentum transfer is dominant in all regimes and is oriented toward the walls. These features are very different from those of a flow driven by a pressure gradient: in this case, momentum flux is oriented toward the walls in the whole fluid volume.

The profile of the density contrast $\langle \delta\rho \rangle$ changes more strongly than that of the velocity from a stepwise variation with $\tilde{z}$ (laminar regime) to a slow linear one (highly turbulent regime). Mass transfer (like the density profile) also depends very much on the flow regime. For laminar flows, transverse mass exchange of fluid in the stable layered region between the fronts is negligible: this is due to the weak mixing efficiency of molecular diffusion and of the residual velocity fluctuations. As a result, the velocity V_f of the displacement front (i.e., far from the measurement window) can be related from mass conservation considerations to the thickness h_0 of the middle layer. As θ increases (or At decreases), h_0 decreases until one observes a counterflow of the two pure fluids without an intermediate layer.

In the turbulent regime, there is an efficient transverse turbulent mixing between the ascending and the descending parts of the flow, particularly at low θ and high At: as a result, the transverse gradient of the mean density over the tube section is small and nearly constant. As shown in Ref. 14, this transverse exchange determines, for a large part, the macroscopic diffusion coefficient characterizing the longitudinal spreading of the mean concentration profile. Unlike for the laminar regime, there is no obvious theoretical relation between the front velocity V_f and the velocity field $u(y,z)$ in flow sections located in the middle part of the tube. However, the experimental data indicate that the two quantities are correlated: the ratio V_f/u_m is nearly constant in the four experimental cases T_i, although 50% lower than for the laminar flows.

Another important characteristic of these flows is their stationarity. In the laminar regime, aside from a few fluctuations, the concentration and velocity profiles can be considered as stationary. In the turbulent regime, there is a quasistationary phase during which the mean velocity profiles can be considered as constant even though the average concentration in the measurement windows drifts with time, due to the spreading of the mean concentration profile. The variations with time of the transverse concentration gradient driving the flow and of the fluctuations of the velocity and concentration are similar but depend on T_i: for $\theta=15°$ ($T1$ and $T3$), they display a quasistationary phase, while for $\theta=30°$ ($T2$ and $T4$), they slowly decay. The better stationarity of the mean velocity may indicate that it reflects an equilibrium of forces along the full mixing zone, while the other quantities are more local.

At θ and At values intermediate between those corresponding to the laminar and developed turbulent regimes, intermittent flows are observed: laminar counterflows of the two fluids accelerate until a turbulent burst is triggered, resulting in strong, transient, transverse mixing. The determination of the stability criteria for the layered flows encountered in the laminar regimes will be necessary in order to 26.dicatefecte.

if Thematiopresent work is on
measuremenns
spomenns

region inside the measurement plane. At higher θ and/or lower At values, the relative influence of viscous and 3D out-of-plane transport terms becomes important.

For a better understanding of these buoyancy driven mixing processes, quantitative measurements of the transverse mass exchange will be needed: simultaneous PIV and LIF measurements will be necessary in order to measure the correlations between velocity and concentration fluctuations, which determines the transverse turbulent mass flux.

ACKNOWLEDGMENTS

We thank C. Borget and R. Pidoux for the design and construction of the experimental setup. We are indebted to Y. Hallez, E. J. Hinch, and J. Magnaudet for their many thoughtful suggestions, to D. Salin for his careful reading of the manuscript and for useful discussions, and to B. Semin for his precious help with the numerical simulations. We thank MENSR for the scholarship supporting the Ph.D. thesis of J. Znaien. This research has been funded by the French ANR through the ANR-07-BLAN-0181 project "GIMIC."

[1]P. Odier, J. Chen, M. K. Rivera, and R. E. Ecke, "Fluid mixing in stratified gravity currents: The Prandtl mixing length," Phys. Rev. Lett. **102**, 134504 (2009).
[2]H. E. Huppert, in *Perspectives in Fluid Dynamics: A Collective Introduction to Current Research*, edited by G. K. Batchelor, H. K. Moffatt, and M. G. Worster (Cambridge University Press, Cambridge, UK, 2000), pp. 447–506.
[3]M. H. I. Baird, K. Aravamudan, N. V. Rama Rao, J. Chadam, and A. P. Peirce, "Unsteady axial mixing by natural convection in a vertical column," AIChE J. **38**, 1825 (1992).
[4]E. E. Zukoski, "A review of flows driven by natural convection in adiabatic shafts," NIST Report No. NIST-GCR-95-679, 1995, and references therein.
[5]S. B. Dalziel, M. D. Patterson, C. P. Caulfield, and I. A. Coomaraswamy, "Mixing efficiency in high aspect-ratio Rayleigh-Taylor experiments," Phys. Fluids **20**, 065106 (2008).
[6]J. E. Simpson, "Gravity currents in the laboratory, atmosphere and ocean," Annu. Rev. Fluid Mech. **14**, 213 (1982).
[7]J. E. Simpson, *Gravity Currents in the Environment and the Laboratory*, 2nd ed. (Cambridge University Press, Cambridge, UK, 1997).
[8]H. E. Huppert, "Gravity currents: A personal review," J. Fluid Mech. **554**, 299 (2006).
[9]R. E. Britter and P. F. Linden, "The motion of the front of a gravity current travelling down an incline," J. Fluid Mech. **99**, 531 (1980).
[10]D. I. H. Barr, "Densimetric exchange flows in rectangular channels," Houille Blanche **22**, 619 (1967).
[11]J. O. Shin, S. B. Dalziel, and P. F. Linden, "Gravity currents produced by lock exchange," J. Fluid Mech. **521**, 1 (2004).
[12]V. K. Birman, B. A. Battandier, E. Meiburg, and P. F. Linden, "Lock-exchange flows in sloping channels," J. Fluid Mech. **53**, 1 (2007).
[13]T. Séon, D. Salin, J. P. Hulin, B. Perrin, and E. J. Hinch, "Buoyancy-driven miscible front dynamics in tilted tubes," Phys. Fluids **17**, 031702 (2005).
[14]T. Séon, J. Znaien, E. J. Hinch, B. Perrin, D. Salin, and J. P. Hulin, "Front dynamics and macroscopic diffusion in buoyancy-driven mixing in a tilted tube," Phys. Fluids **19**, 125105 (2007).
[15]J. Znaien, Y. Hallez, F. Moisy, J. Magnaudet, J. P. Hulin, D. Salin, and E. J. Hinch, "Experimental and numerical investigations of flow structure and momentum transport in a turbulent buoyancy-driven flow inside a tilted tube," Phys. Fluids **21**, 115102 (2009).
[16]T. Séon, J. P. Hulin, D. Salin, B. Perrin, and E. J. Hinch, "LIF measurements of buoyancy-driven mixing in tilted tubes," Phys. Fluids **18**, 041701 (2006).
[17]B. C. Kneller, S. J. Bennett, and W. D. McCaffrey, "Velocity structure, turbulence and fluid stresses in experimental gravity currents," J. Geophys. Res. **104**, 5381 (1999).
[18]B. Kneller and C. Buckee, "The structure and fluid mechanics of turbidity currents: A review of some recent studies and their geological implications," Sedimentology **47**, 62 (2000).
[19]T. Séon, J. Znaien, E. J. Hinch, B. Perrin, D. Salin, and J. P. Hulin, "Transient buoyancy-driven front dynamics in nearly horizontal tubes," Phys. Fluids **19**, 123603 (2007).
[20]Y. Hallez and J. Magnaudet, "Turbulence-induced secondary motion in a buoyancy-driven flow in a circular pipe," Phys. Fluids **21**, 081704 (2009).
[21]J. E. Simpson and R. E. Britter, "The dynamics of the head of a gravity current advancing over a horizontal surface," J. Fluid Mech. **94**, 477 (1979).
[22]C. Härtel, E. Meiburg, and F. Necker, "Analysis and direct numerical simulation of the flow at a gravity-current head. Part 1. Flow topology and front speed for slip and no-slip boundaries," J. Fluid Mech. **418**, 189 (2000).
[23]F. H. Champagne, V. G. Harris, and S. Corrsin, "Experiments on nearly homogeneous turbulent shear flow," J. Fluid Mech. **41**, 81 (1970).
[24]S. Tavoularis and S. Corrsin, "Experiments in nearly homogenous turbulent shear flow with a uniform mean temperature gradient. Part 1," J. Fluid Mech. **104**, 311 (1981).
[25]S. Tavoularis and U. Karnik, "Further experiments on the evolution of turbulent stresses and scales in uniformly sheared turbulence," J. Fluid Mech. **204**, 457 (1989).
[26]B. E. Launder and D. B. Spalding, *Lectures in Mathematical Models of Turbulence* (Academic Press, London, 1972).
[27]S. B. Pope, *Turbulent Flows* (Cambridge University Press, Cambridge, UK, 2000).